

0.8–13 MICRON SPECTROSCOPY OF V838 MONOCEROTIS AND A MODEL FOR ITS EMISSION

DAVID K. LYNCH,¹ RICHARD J. RUDY, RAY W. RUSSELL,¹ S. MAZUK, CATHERINE C. VENTURINI, AND W. DIMPFEL
 The Aerospace Corporation, P.O. Box 92957, Los Angeles, CA 90009

LAWRENCE S. BERNSTEIN
 Spectral Sciences, Inc., 4 Fourth Avenue, Burlington, MA 01803

MICHAEL L. SITKO¹
 Department of Physics, University of Cincinnati, Cincinnati, OH 45221

SERGIO FAJARDO-ACOSTA¹
 Spitzer Science Center, California Institute of Technology, MC 314-6, Pasadena, CA 91125

ALAN TOKUNAGA
 Institute for Astronomy, University of Hawaii, 2680 Woodlawn Drive, Honolulu, HI 96822

ROGER KNACKE¹
 School of Science, Pennsylvania State University at Erie, Station Road, Erie, PA 16563

RICHARD C. PUETTER
 University of California, San Diego, 9500 Gilman Drive, La Jolla, CA 92093; and Pixon LLC, 9295 Farnham Street, San Diego, CA 92193

AND

R. BRAD PERRY¹
 NASA Langley Research Center, MS 160, Hampton, VA 23681
 Received 2003 July 21; accepted 2004 January 9

ABSTRACT

We report on the results of a number of infrared spectra (0.8–2.5, 2.1–4.6, and 3–14 μm) of V838 Monocerotis, taken from a short time after discovery in 2002 January to about 14 months later, in early 2003. The spectrum evolved dramatically, changing from a quasi-photospheric stellar spectrum with weak atomic emission lines (some with P Cygni profiles) to one showing a wide range of deep absorption features indicative of a cool, extended atmosphere with a circumstellar dust shell. The early spectra showed lines of *s*-process elements, such as Sr II and Ba I. The later spectra showed absorption by gaseous H₂O, CO, AlO, TiO, SiO, SO₂, OH, VO, and SH, as well as a complex of emission near 10 μm reminiscent of silicate emission, with a central absorbing feature at 10.3 μm . Thus, V838 Mon appears to be oxygen-rich. A simple, spherically symmetric model of the system involving a central star with a two-component expanding circumstellar shell is presented that is able to explain the major molecular features and spectral energy distribution in the object's late stages. The derived shell mass and distance are 0.04 M_{\odot} and 9.2 kpc, respectively.

Subject headings: infrared: stars — nuclear reactions, nucleosynthesis, abundances — stars: individual (V838 Monocerotis) — stars: variables: other

1. INTRODUCTION

Since its discovery in early 2002 (Brown 2002), V838 Monocerotis has displayed such dramatic changes in its spectrum that it may well define a new class of objects (Kimeswenger et al. 2002). V838 Mon was originally thought to be a nova, and indeed its spectrum showed a nova-like, F-type continuum, with hydrogen emission lines and neutral and ionized metals. Many lines displayed P Cygni profiles (Munari, Desidera, & Henden 2002a; Lynch et al. 2002b). Most remarkable of all, *s*-process elements were seen in optical spectra (Wagner, Starrfield, & Hauschildt 2002; Kammerer et al. 2002; Iijima & Della Valle 2002; Zwitter & Munari 2002), and it was soon realized that the star was behaving in a very “un-nova-like” way. The spectrum shifted to a cooler, lower excitation one rather than following a normal nova's development, in which the spectrum shows ever-increasing

levels of excitation and ionization. Virtually all of the atomic lines disappeared, and the continuum became dominated by strong molecular absorption (Geballe et al. 2002; Banerjee & Ashok 2002; Sitko et al. 2003), indicative of a spectral type that Desidera & Munari (2002) aptly described as “later than . . . M10 III.” A few months after the outburst, V838 Mon was found to be part of a binary system, with the companion being a B3 V star (Desidera & Munari 2002; Wagner & Starrfield 2002). Infrared observations interspersed with our own and covering the 1–2.5 μm region have been reported by Evans et al. (2003), who speculate that V838 Mon may be an L giant, an interesting possibility in view of the object's low temperature and pressure.

The light curve was also peculiar (Fig. 1), displaying two and perhaps three rapid increases in brightness (hours or days) followed by slower declines (over periods of days). At least one of the declines was probably due to dust formation (Crause et al. 2003), and perhaps all of them were. In light of the complex structure indicated by the *Hubble Space Telescope* (HST) images (Bond et al. 2003), multiple ejection events over

¹ Visiting Astronomer, NASA Infrared Telescope Facility, which is operated by the University of Hawaii under contract with the National Aeronautics and Space Administration.

Report Documentation Page			Form Approved OMB No. 0704-0188		
Public reporting burden for the collection of information is estimated to average 1 hour per response, including the time for reviewing instructions, searching existing data sources, gathering and maintaining the data needed, and completing and reviewing the collection of information. Send comments regarding this burden estimate or any other aspect of this collection of information, including suggestions for reducing this burden, to Washington Headquarters Services, Directorate for Information Operations and Reports, 1215 Jefferson Davis Highway, Suite 1204, Arlington VA 22202-4302. Respondents should be aware that notwithstanding any other provision of law, no person shall be subject to a penalty for failing to comply with a collection of information if it does not display a currently valid OMB control number.					
1. REPORT DATE MAY 2004		2. REPORT TYPE		3. DATES COVERED 00-00-2004 to 00-00-2004	
4. TITLE AND SUBTITLE 0.8-13 Micron Spectroscopy of V838 Monocerotis and a Model for Its Emission				5a. CONTRACT NUMBER	
				5b. GRANT NUMBER	
				5c. PROGRAM ELEMENT NUMBER	
6. AUTHOR(S)				5d. PROJECT NUMBER	
				5e. TASK NUMBER	
				5f. WORK UNIT NUMBER	
7. PERFORMING ORGANIZATION NAME(S) AND ADDRESS(ES) The Aerospace Corporation,PO Box 92957,Los Angeles,CA,90009				8. PERFORMING ORGANIZATION REPORT NUMBER	
9. SPONSORING/MONITORING AGENCY NAME(S) AND ADDRESS(ES)				10. SPONSOR/MONITOR'S ACRONYM(S)	
				11. SPONSOR/MONITOR'S REPORT NUMBER(S)	
12. DISTRIBUTION/AVAILABILITY STATEMENT Approved for public release; distribution unlimited					
13. SUPPLEMENTARY NOTES					
14. ABSTRACT see report					
15. SUBJECT TERMS					
16. SECURITY CLASSIFICATION OF:			17. LIMITATION OF ABSTRACT	18. NUMBER OF PAGES 14	19a. NAME OF RESPONSIBLE PERSON
a. REPORT unclassified	b. ABSTRACT unclassified	c. THIS PAGE unclassified			

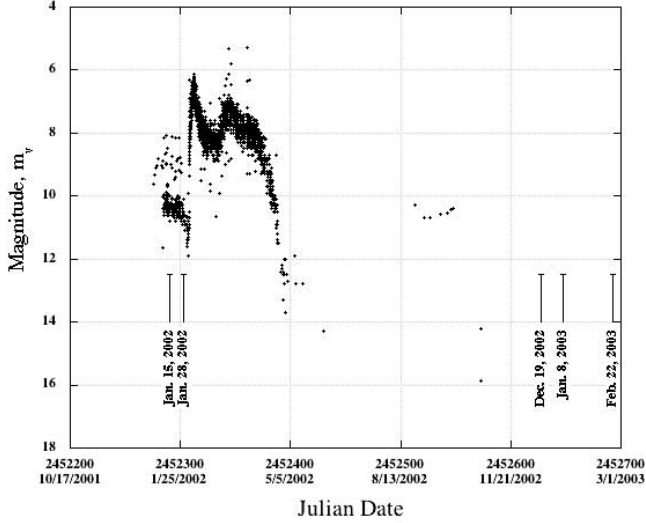


FIG. 1.—Light curve of V838 Mon and times of our observations. The outburst of V838 Mon was discovered in early January of 2002, when it had risen to around the 10th magnitude. It subsequently brightened, reaching about the 6.5th magnitude, then declined moderately, after which it brightened again to around the 7th magnitude. Following this peak, the decline began slowly and accelerated until the curve dropped below the 13th magnitude.

a period of hundreds or thousands of years may be part of V838 Mon's history.

V838 Mon's behavior has so far eluded explanation or parallel. Soker & Tytenda (2003) proposed a stellar merging event (see also Kato 2003), but this would seem untenable in view of the apparent recurrent ejection episodes evidenced by the *HST* imagery (Bond et al. 2003). The similarities between V838 Mon's behavior and that of M31 RV (Rich et al. 1989), V4334 Sgr (Evans, Smalley, & Kimeswenger 2002), and V4332 Sgr (Martini et al. 1999) have been noted by several groups (Wagner et al. 2002b; Kimeswenger et al. 2002; Munari et al. 2002b; Bond et al. 2003). Retter & Marom (2003) suggest that the object's observed behavior could be explained by an expanding central red giant that enveloped three relatively massive planets in close orbits. It is interesting to note that each of the above-mentioned scenarios involves an evolved object, probably an asymptotic giant branch (AGB) star, and quite likely in a binary system.

In this paper we document the extraordinary spectral development of V838 Mon across a broad range of wavelengths and time periods, starting within days of its discovery.

2. OBSERVATIONS

Table 1 lists the dates of our observations, the instruments used, and the telescopes. We took advantage of two close-

in-time observing runs to obtain two sets of spectra, the first using the Broadband Array Spectrograph (BASS; 3–14 μm) and the Near Infrared Imaging Spectrograph (NIRIS; 0.8–2.5 μm), the second using these instruments and SpeX (Rayner et al. 2003). We assumed that the observations were sufficiently close in time to warrant joining them together to obtain much broader wavelength coverage than is possible with a single instrument. This technique we have successfully used before, most recently on another unusual variable star, V4334 Sgr (Lynch et al. 2002b). We collectively refer to the first two spectra, from 2002 January, as the “early” spectrum and the combined observations from 2002 December through 2003 March as the “late” spectrum. Except for a slight change in brightness, we found no significant spectral differences between the two BASS spectra obtained in 2003 January and February, or the two SpeX spectra obtained in 2003 February and March, but we list the observation here for completeness.

BASS and its operation have been described many times before (Hackwell et al. 1990). BASS has a single aperture about 3.3 in diameter on NASA's Infrared Telescope Facility (IRTF), through which all of the starlight passes and is recorded simultaneously at all wavelengths by the 116 back-illuminated blocked impurity band (BIB) Si:As detectors. The calibrator for the BASS observations was α CMa. We assumed that it had a magnitude of -1.41 throughout BASS's wavelength coverage.

NIRIS and its operation on the Lick 3 m telescope have also been described before (Rudy, Puetter, & Mazuk 1999). For these observations we used a 2" wide slit oriented north-south. The only detectable emission was at the star's position, so we believe the spectra to be uncontaminated by the preexisting shell, except perhaps along the precise line of sight (LOS) of the star. For logistic reasons, two different calibrators were used. HR 2007 ($m_v = 5.97$, G4 V) was used in 2002 January, and HR 2779 ($m_v = 5.91$, F8 V) was used in 2002 December (Hoffleit & Jaschek 1982). The intrinsic continuum of both HR stars was assumed to match those models from Kurucz (1994) appropriate to their spectral types and luminosity class. Small adjustments were made to the width and strength of the stronger stellar absorption features (e.g., the calcium infrared triplet and the Paschen lines) in the models to match the actual observations. An absolute flux scale was determined by normalizing to the K magnitudes, which were calculated from the V magnitudes and the $V-K$ color for stars of their respective spectral types tabulated by Koornneef (1983). The dates of our observations relative to the light curve are shown in Figure 1.

The SpeX observations (Table 1) were made at the IRTF on the nights of 2003 February 22 and March 4 UT, using the A0 V star HR 3314 as the calibrator. We assumed that the spectral shape was the same as that of the Kurucz (1994) model for an A0 V star and then scaled the entire spectrum by

TABLE 1
OBSERVATION LOG

UT Date	Julian Date	Instrument	Observatory	Calibrator	Name
2002 Jan 15.5.....	2,452,290.0	BASS	IRTF 3 m	α CMa	Early
2002 Jan 28.2.....	2,452,302.7	NIRIS	Lick 3 m	HR 2007	Early
2002 Dec 19.3.....	2,452,627.8	NIRIS	Lick 3 m	HR 2779	Late
2003 Jan 8.4.....	2,452,647.9	BASS	IRTF 3 m	α CMa	Late
2003 Feb 20.4.....	2,452,690.9	BASS	IRTF 3 m	α CMa	Late
2003 Feb 22.....	2,452,692.5	SpeX	IRTF 3 m	HR 3314	Late
2003 Mar 4.....	2,452,702.5	SpeX	IRTF 3 m	HR 3314	Late

the B and V magnitudes from the Bright Star Catalogue. We show only the 2003 February observations in this paper because they were closest in time to the NIRIS and BASS observations. There was no significant difference between the two SpeX spectra.

3. SPECTRAL ENERGY DISTRIBUTIONS (SEDs)

The overall shape of the early (2002 January) spectrum (Fig. 2) closely matched that of a 2700 K graybody (M5 star) over the observed wavelength range. This suggests that the body was quasi-photospheric. The $10\ \mu\text{m}$ region fell slightly above the graybody curve. There is a suggestion of an upturn at long wavelengths, indicative of thermal emission from dust, but we cannot be certain of this. There is also a possibility that H_2O rotational structure and metal oxide emission are at work here.

At wavelengths of less than about $2.5\ \mu\text{m}$, the spectrum appeared quasi-photospheric, in the sense that it approximated a blackbody, but there was significant continuum structure that is not seen in M-type stars (Fig. 3). Whether this broad continuum structure was absorption or emission is unclear. If there are absorption features at around 0.96 , 1.14 , and $1.5\ \mu\text{m}$, then their close association with H_2O band absorptions, seen later in the object's life, suggests that even as early as 2002 January, H_2O may have begun to form. The feature with the highest contrast appeared as excess emission near $1.6\ \mu\text{m}$, suggestive of the H^- opacity minimum (John 1988), like those seen in late-type stars and galaxies (Wright, Eisenhardt, & Fazio 1994).

About a year later (Fig. 4), the NIR brightness ($0.8\text{--}2.5\ \mu\text{m}$) had increased by roughly a factor of 2, while the long-wavelength IR (LWIR; $8\text{--}13\ \mu\text{m}$) had increased by about a factor of 20. The J , H , K_{short} , L , M , and N magnitudes of the object went from 7.1 , 6.3 , 5.9 , 5.2 , 5.2 , and 4.5 to 6.8 , 5.8 , 4.7 , 2.8 , 2.5 , and 1.5 , respectively. This enormous increase in the LWIR flux and the consequent development of a strong infrared excess probably meant that dust had condensed around the object. Alternatively, the elevated continuum could have meant that molecular features were also shaping the structure at $10\ \mu\text{m}$, a subject that we discuss in more detail below. The late

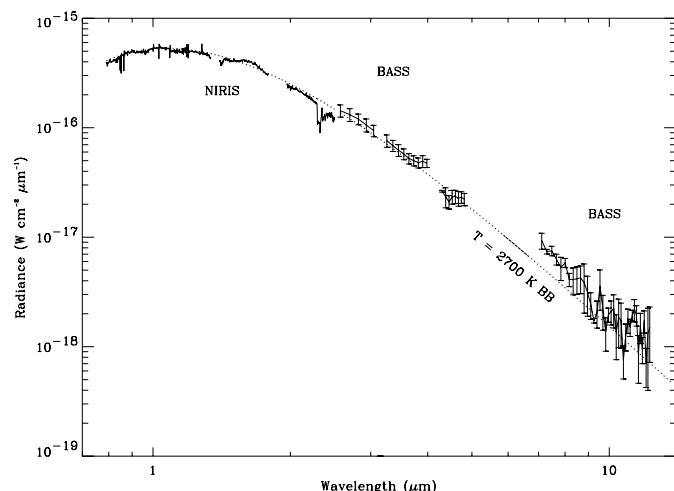


FIG. 2.—Combined 2002 January NIRIS and BASS spectra (early spectrum). The SED followed a roughly Planckian curve, with a temperature of around 2700 K. Except for the emission lines at shorter wavelengths, the only clearly identifiable feature is the strong absorption at $2.3\ \mu\text{m}$ due to CO in the object. The long-wavelength emission fell slightly above the 2700 K graybody curve, perhaps indicative of early dust formation.

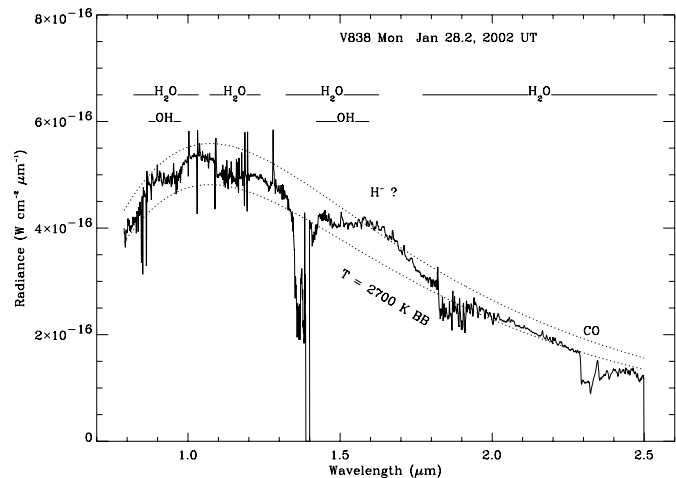


FIG. 3.—2002 January NIRIS spectrum (early spectrum), with graybodies passing through the upper and lower portions. The spectrum is clearly photospheric, although there are a large number of emission features, most of which are the red emission in P Cygni profiles. An excess emission appears near $1.6\ \mu\text{m}$ and may be due to H^- emission at the opacity minimum. Clearly present are the $2.3\ \mu\text{m}$ first-overtone band in absorption and two other continuum depressions, near 0.95 and $1.15\ \mu\text{m}$.

spectrum could not be approximated by a single-temperature blackbody. At short wavelengths, a blackbody of about 2000 K fitted the continuum but fell well below the longer wavelength emission. At longer wavelengths ($8\text{--}13\ \mu\text{m}$), the continuum was well fitted by 650–800 K graybodies.

4. THE EARLY SPECTRUM (2002 JANUARY)

The spectrum showed weak H I Paschen and Brackett emission lines (Table 2), indicative of a thin shell or wind, or possibly a vigorous chromosphere (Fig. 5). No H I P Cygni profiles were seen. Measurements of six well-formed P Cygni lines shortward of $1.3\ \mu\text{m}$ showed a separation of the absorption and emission peaks of $540 \pm 140\ \text{km s}^{-1}$. The FWHM of the absorption and emission components matched the

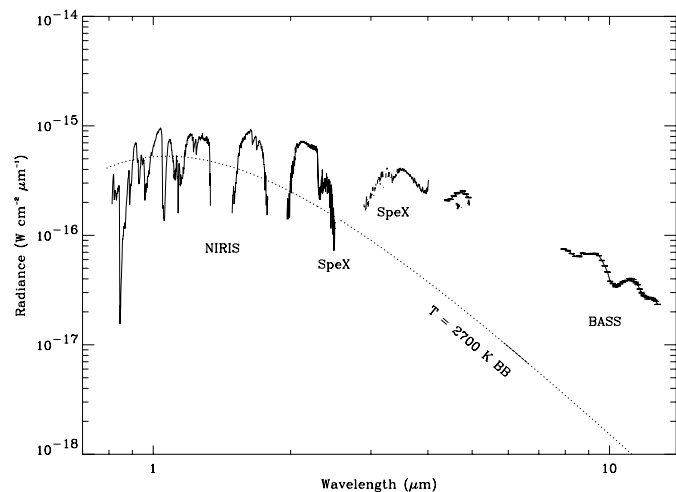


FIG. 4.—2002 December NIRIS, 2003 January BASS, and 2003 February SpeX spectra (late spectrum). V838 Mon had changed enormously, brightening at every wavelength and showing strong molecular features. Clearly present are H_2O , CO, and silicate emission, with a central absorption feature. The 2700 K blackbody from Fig. 2 is also plotted here. A 2000 K graybody does a tolerable job of fitting the $0.8\text{--}2.5\ \mu\text{m}$ continuum but still falls well below the longer wavelength emission.

TABLE 2
2002 JANUARY NIRIS LINE LIST

Measured Wavelength (μm)	ID	Flux ($\text{W cm}^{-2} \mu\text{m}^{-1}$)	$F/F(\text{Pa}\beta)$	Comments
0.8032.....		
0.8061.....		
0.8218.....		
0.8255.....		
0.8300.....		5.880E-20	0.207	
0.8363.....		6.879E-20	0.243	
0.8468.....	Ca II 0.8498	1.766E-19	0.623	
0.8511.....	Ca II 0.8542	2.111E-19	0.744	Red emission
0.8537.....		
0.8550.....	Ba I 0.8560	
0.8603.....		
0.8629.....		1.468E-19	0.518	Red emission
0.8653.....		
0.8666.....	Ca II 0.8662	6.661E-20	0.235	Red emission
0.8687.....	Sr II?	
0.8792.....		1.371E-20	0.048	P Cygni-like
0.8829.....		
0.9000.....	H I Pa10 0.9015	4.318E-20	0.152	Emission
0.9045.....		
0.9071.....		
0.9105.....		
0.9132.....		
0.9211.....		
0.9521.....	H I Pa ϵ 0.9545	1.209E-19	0.426	Emission
0.9566.....		
0.9608.....	Ba I 0.9608	
0.9647.....		
0.9676.....		
0.9703.....		
0.9753.....		
0.9792.....		
0.9882.....		
1.0014.....		
1.0008.....	Sr II 1.0037	3.764E-19	1.327	P Cygni absorption
1.0022.....	Sr II 1.0037	4.254E-19	1.500	P Cygni emission
1.0297.....		
1.0303.....	Sr II 1.0327	3.044E-19	1.073	P Cygni absorption
1.0311.....	Sr II 1.0327	2.022E-19	0.713	P Cygni emission
1.0388.....		8.897E-20	0.314	Emission
1.0445.....		
1.0559.....		
1.0672.....		
1.0882.....		
1.0885.....	Sr II 1.0914	2.086E-19	0.736	P Cygni absorption
1.0910.....	Sr II 1.0914	2.108E-19	0.743	P Cygni emission
1.1280.....	O I 1.1287	3.088E-20	0.109	Emission
1.1411.....		?
1.1581.....		7.944E-20	0.280	Emission
1.1626.....		7.256E-20	0.256	Emission
1.1649.....		
1.1658.....		9.053E-20	0.319	P Cygni absorption
1.1677.....		1.032E-19	0.364	P Cygni emission
1.1774.....		1.087E-19	0.383	Emission
1.1797.....		
1.1848.....		
1.1850.....		2.784E-19	0.982	P Cygni absorption
1.1871.....		3.087E-19	1.089	P Cygni emission
1.1944.....		
1.1942.....		1.010E-19	0.356	P Cygni absorption
1.1960.....		1.323E-19	0.467	P Cygni emission
1.2012.....		
1.2802.....	H I Pa β 1.2818	2.836E-19	1.000	Emission
1.2864.....		
1.3097.....		

TABLE 2—Continued

Measured Wavelength (μm)	ID	Flux ($\text{W cm}^{-2} \mu\text{m}^{-1}$)	$F/F(\text{Pa}\beta)$	Comments
1.3154.....		
1.5053.....	Ba I 1.4999?	1.201E-19	0.423	Emission
1.5627.....		1.438E-19	0.507	Emission
1.5787.....		2.418E-19	0.853	Emission
1.6202.....		1.035E-19	0.365	Emission
1.6417.....	H I Br12 1.6407	1.367E-19	0.482	Emission
1.6735.....		6.487E-20	0.229	Emission
1.7040.....		
1.7102.....		1.027E-19	0.362	Emission
1.7338.....	H I Br10 1.7362	1.541E-19	0.543	Emission
1.7837.....		
1.7899.....		
1.7996.....		
1.8217.....		1.911E-19	0.674	Emission
1.9360.....		
1.9547.....		
1.9762.....		
2.0018.....		
2.0191.....		5.426E-20	0.191	Emission
2.0530.....		6.386E-20	0.225	Emission
2.0669.....		5.576E-20	0.197	Emission
2.1050.....		2.258E-20	0.080	Emission
2.1638.....	H I Br γ 2.1655	5.047E-20	0.178	Emission
2.1777.....		3.356E-20	0.118	Emission
2.1895.....		2.444E-20	0.086	Emission
2.2040.....		8.387E-20	0.296	Emission
2.2248.....		6.340E-20	0.224	Emission
2.2636.....		2.634E-20	0.093	Emission

NOTES.—There are many weak lines to be measured. All lines are in absorption unless otherwise noted.

instrumental resolution ($0.0016 \mu\text{m}$ at Paschen wavelengths, or about 480 km s^{-1}), indicating that the lines were too narrow to be resolved, probably less than about 200 km s^{-1} .

There were six strong lines in our early spectrum that we could not readily identify: 1.0022, 1.0303, 1.0941, 1.1861, 1.1950, and $1.5006 \mu\text{m}$. In view of the early *s*-process elements reported in § 1, we corrected for the observed radial

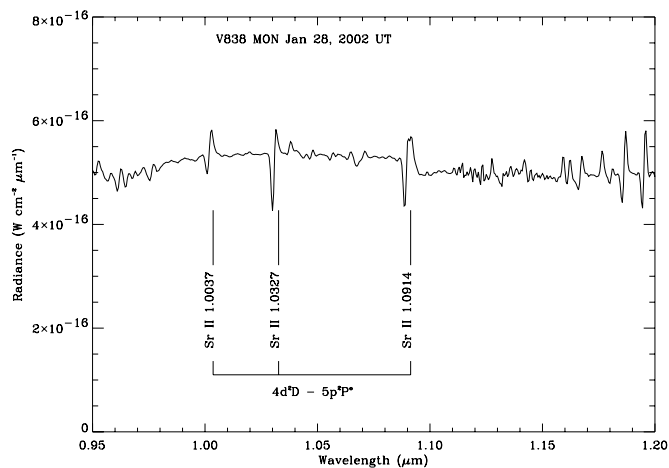


FIG. 5.—Enlargement of part of Fig. 3 (early spectrum) showing the complexity of the spectrum. Some lines are in absorption, others are in emission, and still others show both, in the form of the P Cygni profiles. Three of the strongest P Cygni lines are from the Sr II $4d^2D-5p^2P^o$ multiplet. The H I lines are weak, and both Pa γ and Pa δ slightly contaminate the Sr II lines, the former of which is evident as a “doubled” emission feature in the blend with Sr II $1.0914 \mu\text{m}$.

velocity and found that three of the lines were attributable to an Sr II $4d^2D-5p^2P^o$ multiplet: 1.0037, 1.0327, and $1.0914 \mu\text{m}$ (Fig. 5). All three showed strong P Cygni profiles. Two were slightly contaminated by emission from H I Pa γ and Pa δ . Sr II $0.8689 \mu\text{m}$ also appeared to be present, although weakly. Ba I $1.5053 \mu\text{m}$ may be responsible for the strong line at $1.5000 \mu\text{m}$ and weaker lines at 0.9608 and $1.008 \mu\text{m}$. It is also possible that the Ba I $1.0032 \mu\text{m}$ line was blended with Sr II $1.0037 \mu\text{m}$. Unfortunately, the confirming persistent lines of Ba I expected at 2.3254 and $2.5514 \mu\text{m}$ fall in the object’s CO first-overtone band and the Earth’s terrestrial water band, respectively. The origins of the strong lines at 1.1861 and $1.1950 \mu\text{m}$ remain unknown, but they may well provide some crucial information about the object.

There were also a large number of weak lines in our spectrum whose presence was certain but whose exact shape and wavelengths could not be readily specified. This was because of the frequently occurring P Cygni-like structures that made it difficult to isolate the lines and separate one from another so that a local continuum could be defined. Most of these lines remain unidentified, despite a thorough search of the National Institute of Standards and Technology (NIST) and other databases. Like the strong lines at 1.1861 and $1.1950 \mu\text{m}$, many of the weak lines are probably due to *s*-process or other exotic species, and these will contain important information about V838 Mon’s composition and history.

Between 3 and $13 \mu\text{m}$, the spectrum followed the 2700 K continuum reasonably well, although there was some indication of a weak IR excess in the $8-13 \mu\text{m}$ region. The spectrum also showed possible evidence of a weak absorption feature centered at $9.2 \mu\text{m}$. We did not observe the emission features at

11.3, 11.6, and 12.8 μm ([Ne II]) or a 10%–15% silicate absorption feature seen by Käufl et al. (2002) on 2002 February 9.

5. THE LATE SPECTRUM (2002 DECEMBER–2003 JANUARY)

By 2002 December, only the CO first-overtone band at 2.3 μm was recognizable from the early spectrum (Figs. 6 and 7). The late spectrum was dominated by molecular bands (Tables 3, 4, and 5), the most prominent of which are the H₂O and CO bands. Of particular interest were the AlO and VO features. These were the $A-X(4, 0)$ doublet, peak absorption at 1.225 and 1.244 μm , and the $A-X(2, 0)$ doublet at 1.650 and 1.687 μm . The other AlO $A-X$ bands in the vibrational sequence were less evident because of masking by much stronger water features. A very deep, broad absorption at 1.05 μm was tentatively identified as a combination of the AlO $A-X(6, 0)$ transition and the vanadium oxide (VO) $A-X(0, 0)$ feature seen in the spectra of late-type stars. Because the AlO and VO features arise directly from the ground electronic vibration level, they can exhibit strong absorption at the atypically low temperature (approximately 600 K) indicated by the water and CO spectral absorption profiles. Other VO features were also evident, including the $A-X(1, 0)$ 0.960 μm , (2, 0) 0.888 μm , and (3, 0) 0.822 μm bands and the $B-X(0, 0)$ 0.797 μm and (0, 1) 0.847 μm bands (these wavelengths correspond to the observed minima, not the band centers). In contrast, titanium oxide (TiO), which frequently dominates the spectra of late-type stars, was less apparent in these near-infrared data, with only the $E-X(0, 0)$ band at 0.84 μm appearing as an underlying contribution to the stronger VO $B-X(0, 1)$ band.

Figure 8 shows the SpeX spectrum from 2003 February overplotted on the BASS spectrum from 2003 January for the same wavelength region. The BASS spectrum spans a larger wavelength than the SpeX but at a lower spectral resolution. Data points in the SpeX spectrum in which the telluric transmission is less than 80% have been omitted. The two spectral shapes are clearly consistent, although there is a brightness difference, perhaps a result of different observation epochs. Near 2.3 μm the CO first-overtone band is evident as an absorption feature. The spectrum longward of 2.5 μm results from a complex interplay of photospheric and

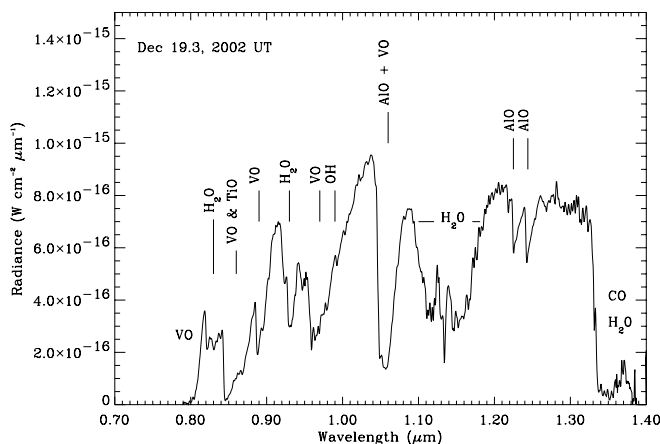


FIG. 6.—Late NIRIS spectrum from 0.81 to 1.33 μm . The spectrum is dominated by H₂O, CO, TiO, OH, VO, and AlO. The red-trending $A-X(4, 0)$ doublet of AlO at 1.225 and 1.244 μm is particularly diagnostic. A number of weaker bands—presumably molecular—are present but are either not readily identifiable or sufficiently broad that they lack discrete features, e.g., OH, HS, and H₂S.

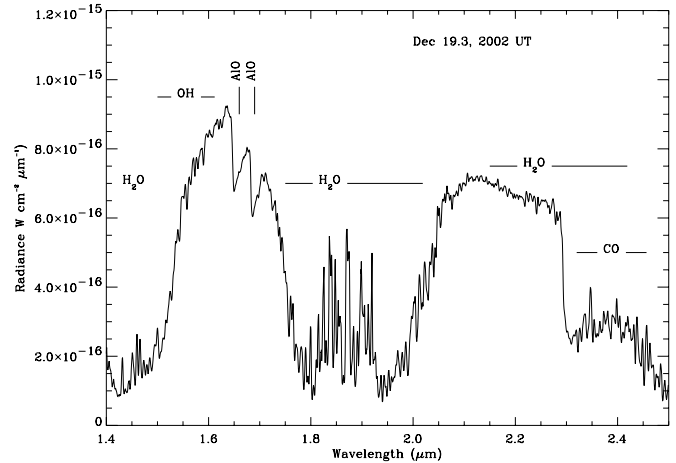


FIG. 7.—Late NIRIS spectrum from 1.4 to 2.5 μm . The spectrum is dominated by H₂O and CO. The red-trending $A-X(2, 0)$ doublet of AlO at 1.650 and 1.687 μm is particularly diagnostic. A number of weaker bands—presumably molecular—are present but are either not readily identifiable or sufficiently broad that they lack discrete features, e.g., OH and HS.

shell molecular absorptions and emissions. Key structures include photospheric OH and SH and shell complexes from H₂O and SiO overtones. The dip around 3.3 μm is due to H₂O ($2\nu_2$).

At longer wavelengths, we observed a 650 K thermal continuum with two emission features, at 9.2 and 11.2 ± 0.2 μm (Fig. 9). Alternatively, the structure could be three absorption features centered at 8.4, 10.3, and 12 μm or possibly a single silicate emission feature transected by silicate absorption. It is interesting to note that V838 Mon's spectrum was not like those of warm stars with a cool shell, i.e., one showing two distinct emission maxima. V838 Mon's spectrum does not show the significant minimum in the 4–8 μm region that would occur between two Planck functions; rather, it remains high throughout the 4–8 μm region.

If there were two separate emission features in the 10 μm window, then the one near 11.2 μm could be attributed to SiC. This, however, seems unlikely. SiC forms when $C/O > 1$, but the object is clearly oxygen-rich, as the abundance of metal oxides seen at short wavelengths shows. In the context of dust, no astrophysically abundant mineral known to us can produce such a feature.

The continuum drawn in Figure 8 could as well have passed through the two peaks, and therefore the structure could represent gas-phase absorptions by molecules. The metal oxides produce strong rovibrational bands in these regions. For

TABLE 3
SUMMARY OF PARAMETERS DETERMINED BY SPECTRAL FITTING OF THE VIS–NIR AND IR DATA

Parameter	Value
Photosphere emission temperature, $T_{\text{BB}, p}$	2100 K
Photosphere outer/inner source ratio, α	0.85
Cloud rotational temperature, T_{rot}^a	650 K
Cloud Doppler velocity spread, Δv_{Dop}^b	50 km s ^{−1}
Cloud emission temperature, $T_{\text{BB}, c}$	750 K
Emission area ratio, A_c/A_p	24
Cloud expansion velocity, v_c^b	250 km s ^{−1}

^a For the VIS–NIR fit it was assumed that $T_{\text{vib}} = T_{\text{rot}}$.

^b Estimated from P Cygni profiles.

TABLE 4
MOLECULAR COLUMN AMOUNTS DETERMINED BY SPECTRAL FITTING OF THE VIS–NIR AND IR DATA

Molecule	Total (molecules cm ⁻²)	Cold Shell Transmittance Scaling Parameter, η^a
Photosphere Molecular Columns		
OH.....	1.0×10^{23}	...
SH.....	2.5×10^{21}	...
Cloud Molecular Columns		
H ₂ O.....	1.6×10^{22}	0.12
CO.....	6.6×10^{21}	0.4
NO.....	2.1×10^{20}	0.7
SiO.....	6.7×10^{20}	0.5
H ₂ S.....	3.5×10^{20}	1.0
SO ₂ (cloud).....	1.8×10^{19}	1.8, 3.0 ^b

^a Fit based on t^η , where t is the transmittance calculated for 10% of the total column amount for each species.

^b Separate values determined for the SO₂ 7.4 and 8.5 μ m bands, respectively.

example, SO₂ can produce an absorption at around 8.4 μ m with the right width, and so too can AlO and FeO at 10.3 μ m.

If the structure were due to silicates, then the underlying emission would appear to be similar to that produced by comets (Hanner, Lynch, & Russell 1994) and circumstellar shells (Waelkens et al. 1999), because it extended from 8.4 to 11.8 μ m. Owing to the presence of the absorption, it was difficult to discern finer structure features, such as the olivine feature at 11.2 μ m. The maximum absorption occurred at 10.3 ± 0.1 μ m and had an FWHM of no more than 1 μ m, although the width is uncertain because we do not know where the peak emission from V838 Mon occurred in this region or how large it was relative to the continuum. The absorption at 10.3 μ m reached below the local continuum. Assuming that the peak emission in Figure 9 would have been about 6.4×10^{-17} W cm⁻² μ m⁻¹ (dotted line) and its value at the depth of the absorption about 3.4×10^{-17} W cm⁻² μ m⁻¹, then the optical depth was about 0.65.

Silicate emission features with central absorptions have been seen before in a number of sources: NML Cyg (Neugebauer, Martz, & Leighton 1965), H II regions (Gillett et al. 1975), supergiant and AGB stars (Speck et al. 2000), and most recently, a number of *Infrared Space Observatory* objects (Molster, Waters, & Tielens 2002a; Molster et al. 2002b, 2002c). In all these cases the absorption is believed to be local to the source rather than interstellar. What sets V838 Mon's feature apart from the others is the fact that the central absorption occurs at 10.3 μ m rather than at 9.7–9.8 μ m, where

most interstellar medium (ISM) and circumstellar absorption reach their maximum. A few sources are known to show a 10.3 μ m feature, most being in emission: some interplanetary dust particles (Sandford & Walker 1985), portions of the η Carinae homunculus (Polomski et al. 1999), exozodiacal emission (Reach et al. 2003), and the broad silicate emission in supergiants and AGBs (Speck et al. 2000). Recently, Lynch, Russell, & Sitko (2002a) reported a weak 10.3 μ m feature in the spectrum of C/1999 T1 (McNaught-Hartley), which they argued may have been due to hydrated silicates. With the apparent abundance of water in V838 Mon's spectrum, the presence of hydrated silicates in V838 Mon's dust shell is a possibility.

6. EXTINCTION

Roche & Aitken (1984, 1985) analyzed the relation between the visual extinction A_V and the silicate optical depth at 9.7 μ m, $\tau_{9.7}$. They found $A_V/\tau_{9.7} = 18$ for the general ISM and $A_V/\tau_{9.7} = 9$ toward the Galactic center. While V838 Mon's peak absorption is at 10.3 μ m, we assume that Aitken and Roche's findings at 9.7 μ m apply here. An optical depth of 0.65, reported above, leads to $5.8 < A_V < 12$ for the above

TABLE 5
QUANTITIES DERIVED FROM THE FIT PARAMETERS

Parameter	Value
Cloud radius, R_c	43 AU
Photosphere radius, R_p	8.8 AU
Distance to V838 Mon, R_{V838}	9.2 kpc
Cloud mass, M_c	0.11 M_\odot
Cloud pressure, P_c	9×10^{-9} atm
Cloud molecular collision rate, z_c	30 s ⁻¹

^a Assumes that cloud width is 20% of R_c .

^b Based on local translational temperature of 650 K and collision cross section with H₂ of 1×10^{-15} cm².

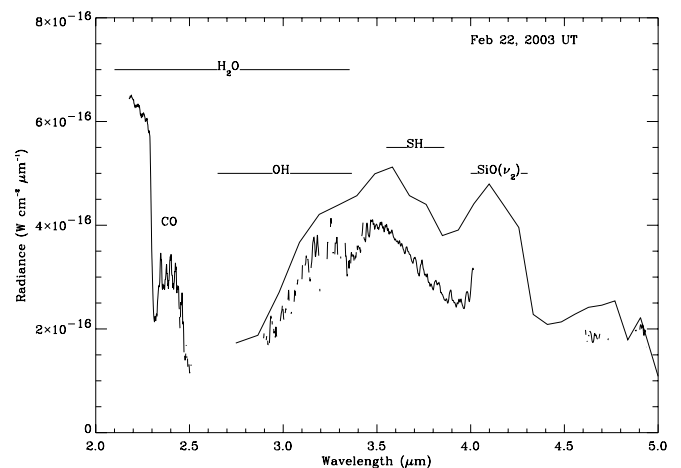


FIG. 8.—2003 February SpeX spectrum (lower curve). The upper curve shows the BASS spectrum taken about a month earlier. At short wavelengths, CO and H₂O are responsible for the decrease longward of 2.3 μ m. The very sharp turn up at 4 μ m is the beginning of the SiO first-overtone band.

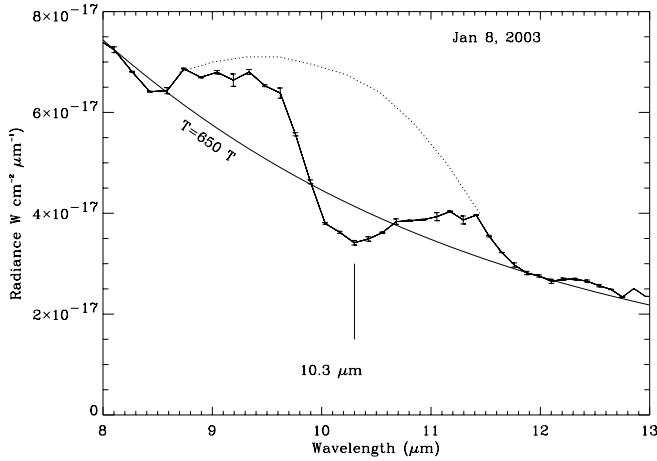


FIG. 9.—The 8–13 μm region of the spectrum taken on 2003 January 8, showing what could be interpreted as two separate emission features, at 9.2 and 11.3 μm . By fitting the continuum to a 650 K blackbody, a more realistic interpretation is found to be a broad silicate emission feature with a central absorption centered at 10.3 μm . This is reinforced by the fact that the center of the absorption falls below the graybody fit. By estimating the silicate emission based on those seen in comets and circumstellar shells (dotted line, approximate), we find a central optical depth of about 0.65. This absorption is almost certainly local to the source and not interstellar, because of the large optical depth. Furthermore, the interstellar absorption peaks near 9.7 μm , while that in V838 Mon peaks at 10.3 μm .

two ratios. Our derived A_V is considerably higher than those reported for about the same time period by Kimeswenger et al. (2002), who found $A_V = 1.8$ and 2.4, respectively. An A_V this large is almost certainly due to extinction from dust near the source from the present outburst or perhaps from some of the dust evident in the *HST* light-echo images (Bond et al. 2003). Indeed, the progenitor of V838 Mon was detected in 1983–1984 as IRAS 07015–0346.

7. MODELING THE SPECTRA

Our model is based on the following observed properties of the source. The central star ejected a shell of material that cooled and became optically thick in many molecular bands (e.g., water) while remaining optically thin in the continuum regions. The inner parts of the shell absorbed much of the central star's radiation and shielded the outer regions from it. Therefore, we model the whole system as a central star with absorption bands and an expanding shell with a cool outer region. Fitting the spectrum requires 11 parameters (radius and temperature of the central star and temperature of the photospheric absorption layer; radius, Doppler width, column density, rotational temperature, and emission temperature of the hot inner part of the shell; and Doppler width, column density, and rotational temperature of the cool outer part of the shell). However, these are not all free parameters, because several are constrained by the observations.

Our analysis is based on the model shown in Figure 10 and has three components: (1) The central star's photospheric emission is modeled as a Shuster-Schwarzschild-like (“two-stream”) emitter in the form of an inner blackbody source with a homogeneous outer, cooler absorbing layer. Key parameters for the central star are radius R_p and temperature for the blackbody $T_{\text{BB},p}$. (2) The hot shell is characterized by a number of parameters, including (a) a Doppler velocity spread Δv_{Dop} , which represents the relative spread in velocities among the various subshells combined here into a single effective shell; (b) a rotational temperature T_{rot} , which determines the spectral

breadth of the molecular absorption profiles; (c) a vibration/blackbody emission temperature $T_{\text{BB},c}$; and (d) column amounts for each molecular species. (3) The cold shell is characterized by the same parameters as the hot shell. For simplicity, however, in this analysis the emission temperature of the cold shell was set to zero, and the velocity spread and rotation temperature were taken to be those of the hot shell. The absorber column amounts were the only quantities varied for the cold layer.

We assumed that the pressure in the cloud is sufficiently low (as discussed below, this is a valid assumption) that the emission temperature is governed by radiative equilibrium between absorption of the stellar source energy and emission to space. In actuality, there is not a well-defined emission temperature. Each molecule is characterized by a nonthermal population distribution of vibration-rotation levels. Furthermore, absorbed stellar photons, which excite these levels, can be reemitted at different wavelengths and then reabsorbed within an optically opaque cloud, which is the situation for V838 Mon. This reemission-reabsorption process can occur many times before the photon exits the cloud. This sort of “multiple scattering” problem is well suited for a Monte Carlo radiation transport treatment, because it facilitates the complexities associated with keeping track of individual quantum states and the changes in the photon wavelength (Duff & Bernstein 1981). In this analysis, we make the simplifying assumption that the emission source function for all the molecules is characterized by a single blackbody temperature, $T_{\text{BB},c}$. This enables a straightforward approximate description of the observed signal to be formulated.

The observed signal for each wavelength range was simulated on the basis of the above physical description, using the following approximate radiative transport expression:

$$I = (A_p / \pi R_{\text{V838}}^2) B(T_{\text{BB},p}) [t_p + \alpha(1 - t_p)] t_{\text{hot}} t_{\text{cold}} + (A_c / \pi R_{\text{V838}}^2) B(T_{\text{BB},c}) (1 - t_{\text{hot}}^2) t_{\text{cold}}, \quad (1)$$

where A is area, B is the blackbody function, t is the photosphere and cloud shell transmittance, α is the ratio of the

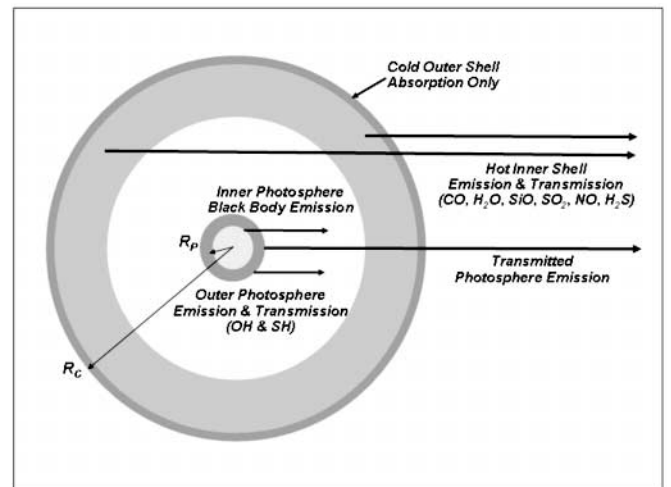


FIG. 10.—Model of V838 Mon's photosphere and its expanding shell used in the analysis of the VIS–NIR and IR data. The ratio of effective-shell to photosphere emitting areas, or equivalently, R_c/R_p , is directly determined by the spectral analysis. The thickness of the cloud and outer photosphere enter into the derivation of physical quantities, such as cloud mass, based on the spectral fit parameters.

emitting area–blackbody products of the outer and the inner photosphere, and R_{V838} is the distance to V838 Mon (see the Appendix for a derivation of eq. [1]). For notational simplicity, the wavelength dependence of the various quantities has been omitted. We noted that the t_{hot}^2 dependence accounts for the emission from the front and back sides of the hot shell. The transmittances were modeled as a product of transmittances for the component molecular species. The species transmittances were obtained from band model radiative transfer (RT) codes (Sundberg, Duff, & Bernstein 1993; Walker, Malkmus, & Ludwig 1981) used to simulate the optically opaque emission-absorption spectra of high-temperature rocket plumes. A Doppler curve of growth was employed for the RT calculations.

The possible presence of silicate dust was not included in the model. As is evident below, the late SED is plausibly explained just in terms of photosphere and cloud molecular emission and absorption. Thus, the extent of dust formation is still an open issue. The early postoutburst extinction observed for the 2002 February and March events, which has been attributed to dust formation, may alternatively be explained by a combination of molecular Rayleigh scattering and molecule formation, i.e., metal oxides, H_2 and H_2O . Based on the retrieved column amounts for the late spectrum, we estimate that the total molecular columns for the early spectrum are of the order of 1×10^{17} molecules cm^{-2} , mostly H_2 . This translates into a Rayleigh-scattering optical depth of ~ 11 at $0.5 \mu\text{m}$, a multiple-scattering regime in which even a small amount of absorption, as would be present in metal oxides and H_2O , will lead to large extinctions. The importance of Rayleigh scattering is substantially reduced for the late spectra because of the lower column density and longer wavelengths analyzed here. For example, at the short-wavelength edge of the NIRIS spectrum ($0.8 \mu\text{m}$), we estimate the Rayleigh extinction optical depth at 0.07.

7.1. The 0.8–2.5 μm Analysis

The initial focus was to identify the molecular features in the gas cloud and to determine their column amounts. For this purpose, the radiance data were converted to transmittance data by dividing by a photosphere blackbody emission curve and scaling the resulting curve to unit transmittance at a wavelength (in this case $2.13 \mu\text{m}$) at which the cloud was presumed to have the highest transmittance. This procedure is based on the further assumption that in the visible-to-NIR (VIS–NIR) spectral region, thermal emission from the cloud is negligible. As detailed below, this is satisfactory for the time frame of ~ 10.5 months from peak outburst considered here; however, both terms in equation (1) would be required for analysis of data within a time frame of several months from the peak outburst. The photosphere blackbody temperature was selected as the temperature that yielded the most spectrally uniform distribution of near-unity window region transmittances. The resulting value was $T_{\text{BB},p} = 2100 \text{ K}$, and the corresponding transmission curve is presented in Figure 11.

Taking the inner-photosphere source to be the dominant source enables a simplified form of equation (1) to be used in the VIS–NIR spectral analysis,

$$I = (A_p / \pi R_{V838}^2) B(T_{\text{BB},p}) t_p t_{\text{hot}} t_{\text{cold}}. \quad (2)$$

It is seen that the molecular contribution enters principally through the total path transmittance, $t_p t_{\text{hot}} t_{\text{cold}}$, without regard to how the transmittance is distributed along the path. For

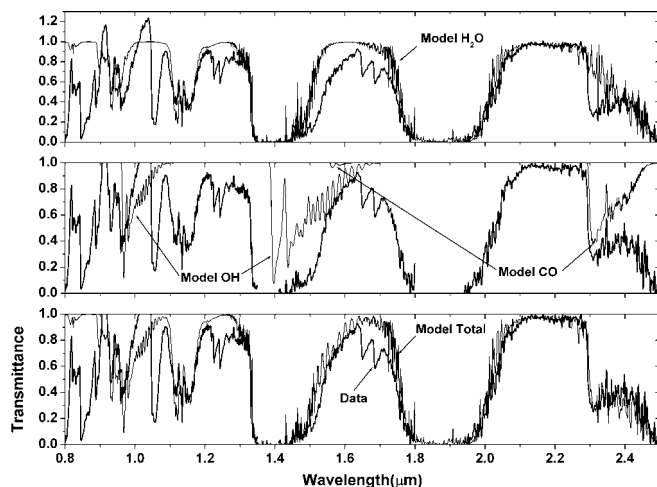


FIG. 11.—Model fit to the VIS–NIR transmission curve, showing the component transmission curves for H_2O (top), CO and OH (middle), and the total model transmittance (bottom). An expanded vertical scale is used for the top panel to indicate that the conversion of the VIS–NIR flux data into transmission data, based on a single-temperature blackbody representation of the photosphere, is somewhat approximate and yields a few features exceeding unit transmittance. We note that there are a number of significant data features in the $0.8\text{--}1.7 \mu\text{m}$ region not accounted for by the model fit (bottom). These correspond to the AlO and VO bands identified earlier (see Figs. 6 and 7), which are not included in the model.

simplicity, in the VIS–NIR spectral fitting we have determined a single equivalent, homogeneous layer (i.e., a single effective temperature and individual species column amounts) that closely approximates the observed transmittances. The transmission curves for the contributing molecular components, OH, H_2O , and CO, as well as the overall fit to the data, are also displayed in Figure 11. The values of the parameters determined by the spectral fits to both the VIS–NIR and the IR data are summarized in Tables 3 and 4. The major features not fitted in the VIS–NIR correspond to the AlO and VO metal oxide bands identified above (see Fig. 6. and 7).

It is important to note that while H_2O absorption dominates the overall appearance of the spectrum, OH is a much more prevalent species in terms of its ~ 6 times larger column amount. This leads to an unusually large derived O/C ratio of 19.5, as compared to a typical solar ratio of ~ 2.4 . Excluding the OH contribution from the estimation of the O/C ratio (i.e., just using the H_2O and CO contributions) yields 3.5, a physically plausible value. This strongly suggests that the OH contribution arises entirely from the outer photosphere and that the H_2O and CO contributions originate primarily from the cloud. This makes chemical sense, since at temperatures in the vicinity of the 2100 K photosphere temperature, one would expect chemical equilibrium to favor OH over H_2O ; in contrast, at the much lower $\sim 650 \text{ K}$ temperature of the cloud, H_2O should be strongly favored. The much higher column amount for OH versus H_2O is a consequence of the much smaller photosphere area over which the OH is spatially distributed. As discussed in more detail below, there is an additional reason to confine OH to the photosphere, as it results in a more plausible estimate of the expelled cloud mass.

The sensitivity of the spectral fit to the assumed values of the key parameters is explored in Figure 12, which shows an expanded portion of the VIS–NIR region to enable the effects of parameter variability to be more easily seen. The effective Doppler velocity spread of $\Delta v_{\text{Dop}} = 50 \text{ km s}^{-1}$ (FWHM) was

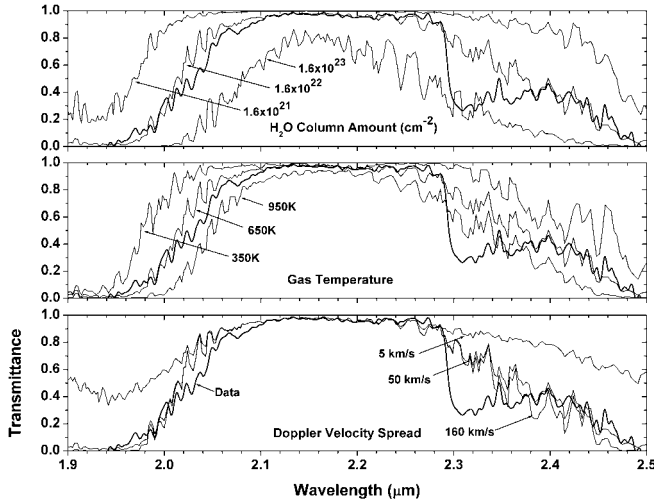


FIG. 12.—Sensitivity of the model transmission predictions in the 1.9–2.5 μm spectral region to variations in the H_2O column amount (*top*), the gas rotation-vibration temperature (*middle*), and the Doppler velocity spread (*bottom*). These calculations only include the H_2O contribution in this spectral region.

selected to be representative of the velocity spreads observed for a wide variety of P Cygni line profiles associated with all three outbursts (Munari et al. 2002b; Osiewala et al. 2004; Wagner & Starrfield 2002). This velocity spread may arguably be on the low side. However, as seen in the sensitivity plot, increasing the velocity spread to 160 km s^{-1} has a minor effect on the modeled transmittance curve. This is because, even at the lower velocity spread, the line widths are sufficiently large that the cloud is largely in the weak-line/Beer's law limit and thus insensitive to increases in the line width (i.e., the lines are highly overlapped). In contrast, a significant decrease in the line width–velocity spread has a dramatic effect on the modeled spectrum. In fact, it would not be possible to achieve a good fit for such a low-velocity spread, as the large increase in column amount required to fit the deeper, more optically opaque regions would lead to a gross overprediction of the absorption in the much more optically thin window regions. The sensitivities to both the gas temperature and column amounts allow a good determination of these quantities. The estimated uncertainty for both of these quantities is $\sim \pm 25\%$ of their fit values.

7.2. The 3–14 μm Analysis

The IR analysis required consideration of all the terms in equation (1), since in this spectral region the emission from a large, cold object can compete with that from a small, hot object. The IR data introduce sensitivity to several additional parameters, including the ratio of emitting areas of the cloud and the photosphere, A_c/A_p , the ratio of emitting area–blackbody products of the outer and the inner photosphere, α , the emission temperature of the hot cloud layer, $T_{\text{BB},c}$, and the presence of a cold, absorbing outer cloud layer. The IR fit was constrained to use the photosphere emission temperature, species column amounts, rotational temperature, and Doppler velocity spread deduced from the VIS–NIR fit. The cold-layer transmittance contribution for each species was separately fitted using the approximation

$$t_{\text{cold}} = t_{10\%}^{\eta}, \quad (3)$$

where $t_{10\%}$ is the transmittance based on 10% of the derived VIS–NIR column amount and η is an adjustable parameter. We assume that the OH and SH contributions are confined to the outer photosphere layer and have adopted a temperature of 1500 K to estimate their transmission and emission spectral distributions. This temperature should be more representative than the 650 K temperature used in the VIS–NIR analysis, which was really driven by the H_2O and CO spectral fits. The depth of the absorption features due to OH and SH is modulated by the η parameter, which is retrieved directly from the data without reference to an assumed outer-photosphere temperature.

Details of the IR spectral fitting are depicted in Figure 13, with the values for the fit parameters summarized in Tables 3 and 4. The most striking aspect of the IR spectral analysis is that it supports the presence of many more molecular species (i.e., SH, SiO, NO, and SO_2) than are observed in the VIS–NIR. They are difficult to ascertain in the VIS–NIR because of both their weaker absorptions and obscuration by the multitude of much stronger and spectrally extensive H_2O , CO, and OH bands. Their effect in the IR is manifested mainly through cold-layer absorption features. The hot layer is sufficiently opaque because of CO and H_2O that adding extra opacity from other species does not introduce additional observable features into the hot-layer source function. It is interesting to note that the 2.5–10 μm region can be adequately explained without invoking the presence of a significant dust layer, although there is a significant amount of dust precursor in the form of molecular SiO. We do not have an assignment for the strong absorption feature in the vicinity of 5 μm , although this may be an artifact of the BASS data, as it does not seem to appear in the SpeX data (see Fig. 13).

There are a number of additional species-specific details employed in the IR spectral analysis. The SH column amount in the outer photosphere was set by scaling the VIS–NIR–determined OH column amount by the S/O solar abundance ratio of 0.022. The total SiO column amount was scaled from the H_2O column amount using the Si/O ratio of 0.042. It is noted that the SiO fundamental at 8.14 μm shows up as an absorption feature, whereas the SiO (2ν) overtone at 4.09 μm appears as an emission feature (i.e., the sharp rise just beyond

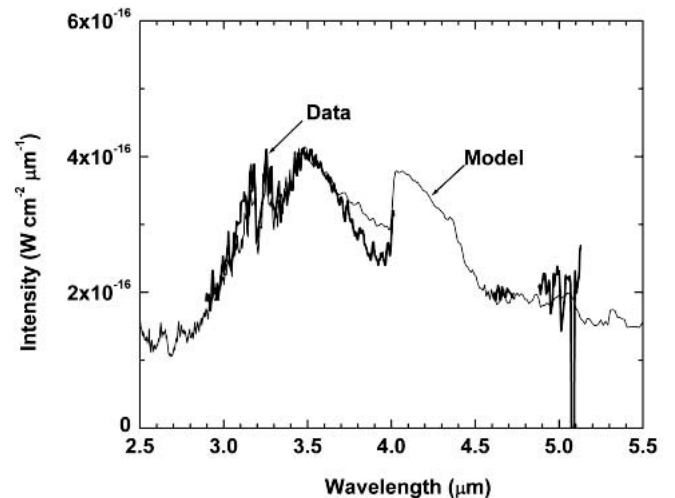


FIG. 13.—Model fit to the SpeX IR flux data. The model fit is that determined from the BASS data, but scaled by a factor of 0.79 to account for the overall intensity difference between the two data sets.

4 μm). This difference in behavior arises from the differences in the relative opacities of the hot and cold layers for the two bands, as is evident from the hot and cold transmission curves in Figure 12. In fitting the SiO (2ν) feature, we had to allow for a slightly increased emission temperature of 790 K, as opposed to the 750 K that seems to characterize the H₂O and CO features. This is not too surprising, as this is a highly nonequilibrium environment. The potential presence of H₂S in the cloud was evaluated using a column amount scaled from H₂O based on the S/O abundance ratio of 0.022. However, because of its extremely weak IR fundamental absorption bands (they are all about 2 orders of magnitude weaker than typical IR bands), no discernible emission or absorption features were evident in the modeled spectrum. In contrast, the much stronger IR bands of SO₂ lead to strong absorption features centered at 7.4 and 8.5 μm , at a total column amount of 5% of that for H₂S. NO shows up in absorption based on a total column amount of 10% of the N/O abundance ratio of 0.21 applied to the H₂O.

The SpeX IR data were obtained at much higher spectral resolution than the BASS data, and their additional spectral detail provides a good consistency check of the BASS-derived spectral fit. The BASS fit is compared to the SpeX data in Figure 13, where good correspondence of the model and observed spectral features is seen. In particular, the identification of the SiO (2ν) overtone emission is further confirmed by the close spectral registration of the sharply rising feature just beyond 4 μm . The only significant difference appears to be a deeper minimum in the data in the SH region at $\sim 3.9 \mu\text{m}$. As the model fits the BASS data well in this region, the difference is ascribed to a difference in the observations. This spectral region is very sensitive to the column amount and temperature of SH in the outer photosphere. Perhaps the difference is due to small temporal variations in these quantities.

The reasonableness of the ratio of cloud and photosphere emitting areas, as well as the cloud emission temperature, can be independently established through consideration of the radiatively driven energy balance of the cloud with the photosphere. If we assume that the cloud emission temperature is dominated by the radiative pumping from the photosphere balanced by radiative emission into space, then a simple means of estimating the cloud temperature follows. Consider a spherical graybody shell surrounding a smaller blackbody source. In the case of V838 Mon, the shell absorbs energy mainly in the VIS–NIR region, where the photosphere emission is strongest, and radiates the absorbed energy at longer wavelengths corresponding to the fundamental bands of the molecular species (i.e., the Einstein A -coefficients for fundamental bands are generally much larger than those for overtone and combination bands). Since at radiative equilibrium the absorbed energy must equal the emitted energy, the temperature of the shell is constrained by

$$\epsilon_c A_c T_{\text{BB},c}^4 = \epsilon_p A_p T_{\text{BB},p}^4, \quad (4)$$

where ϵ_c is the effective emissivity of the cloud in the IR and ϵ_p is the effective emissivity (absorptivity) of the cloud in the VIS–NIR. The effective emissivities correspond to blackbody-weighted averages of the spectral emissivities. They were computed using the VIS–NIR and IR transmittances and emission temperatures derived from the spectral fitting. Solving for $T_{\text{BB},c}$ only depends on the ratio of ϵ and A . From the fits to the VIS–NIR and IR data, we have $\epsilon_p/\epsilon_c = 0.67$, $A_p/A_c = 1/24$, and $T_{\text{BB},p} = 2100 \text{ K}$; thus, $T_{\text{BB},c} = 858 \text{ K}$.

This estimated emission temperature is in reasonable accord with the data-derived value of 750 K.

7.3. Derived Quantities

The derived quantities of most interest, the sizes of the cloud and photosphere, the cloud mass, and the distance to V838 Mon, are all tied to the assumed value of the cloud expansion velocity, v_c . P Cygni observations of the outbursts and postoutburst velocity distributions by us and other groups have indicated a broad distribution of outflow velocities (Munari et al. 2002b; Osiwala et al. 2004; Wagner & Starrfield 2002). However, the general consensus seems to favor a characteristic expansion velocity in the ~ 100 – 400 km s^{-1} range. We have adopted the value $v_c = 250 \text{ km s}^{-1}$ for this analysis but emphasize that the results can be readily scaled if a more appropriate value emerges.

Using the assumed 250 km s^{-1} expansion velocity, the radius of the gas cloud at 10.5 months after the peak outburst, which is the approximate time frame of the later observations analyzed here, is $R_c = 6.9 \times 10^9 \text{ km}$, or 43 AU. Using the spectrally determined cloud-to-photosphere area ratio of 24, the radius of the photosphere is $R_p = 8.8 \text{ AU}$. The mass of the cloud shell is inferred from the total column of O, given by the sum of the H₂O, OH, and CO columns, an assumed solar abundance for O of 7.78×10^{-4} , attributing the rest of the mass to H (presumably in the form of H₂), and the derived cloud radius. The resultant cloud mass, based on an infinitesimal shell thickness, is $0.13 M_\odot$. Assuming a finite thickness of 20% of the shell radius decreases the mass estimate by a factor of 0.81, to $0.11 M_\odot$. As alluded to above, if we associate the OH with the expelled cloud, the mass estimate escalates to $0.76 M_\odot$. This large mass is incompatible with the known characteristics of the progenitor and its apparent multiple outbursts. The distance to V838 Mon follows directly from equation (1), through use of the derived cloud and photosphere areas and spectrally determined temperatures and transmittances to match the observed intensity, and yields $R_{\text{V838}} = 9.2 \text{ kpc}$. Given the column density of H₂ (scaled from the O column), assuming that the thickness of the cloud shell is 20% of its outer radius, and assuming that the 650 K cloud rotational temperature is close to the local gas kinetic temperature, the cloud pressure is estimated to be $9 \times 10^{-9} \text{ atm}$. This low pressure corresponds to a molecular collision rate of $\sim 30 \text{ s}^{-1}$ and is consistent with the assumption of a radiation-driven equilibrium for the emission temperature.

The uncertainties in the derived quantities are largely governed by the uncertainty in the assumed expansion velocity. If we adopt the Hubble distance determination of $\sim 6 \text{ kpc}$ as the gold standard, then this translates into an expansion velocity of 160 km s^{-1} . Recalculation of the derived quantities based on this velocity yields a cloud radius of 28 AU, a photosphere radius of 5.6 AU, and a cloud mass of $0.046 M_\odot$. We note that if instead we base the mass estimate on the carbon column amount set by CO, then the mass estimate is lowered slightly, to $0.031 M_\odot$. Finally, association of the OH with the outer photosphere enables the mass of the outer photosphere to be estimated, resulting in 0.008 – $0.03 M_\odot$ (it depends on the assumed area of the outer photosphere, 1 – $2A_p$). This is in agreement with the estimates made by Evans et al. (2003).

8. LIMITATIONS AND VALIDITY OF THE MODEL

Our approach assumed that the NIR and IR data are consistent with a continuum stellar source and an expanding gas

cloud containing H_2O as the dominant molecular absorber and emitter. The cloud attenuates the stellar emission in the NIR and emits thermally in the IR. All the other modeling details, particularly in regard to the other species, while relevant and significant, are of secondary importance to this central point. There are only three primary free parameters driving the analysis: (1) the total column amount of H_2O in the cloud, (2) an effective vibration-rotation temperature for the H_2O , and (3) the ratio of the cloud and photosphere areas. The NIR spectrum is essentially a transmittance spectrum of the stellar source through the cloud. Fitting of this transmittance spectrum requires, at a minimum, a column amount and an effective temperature for the H_2O . The two parameters derived from the NIR analysis were used as constraints in the IR analysis, which yielded the ratio of cloud and photosphere areas. As discussed later in this section, fitting the finer details of the IR spectrum required adding a colder outer absorbing layer to the cloud and letting the molecular rotation and vibration/emission temperatures differ slightly. The values for the column amounts of these species were physically constrained by their nominal solar abundance ratios relative to O. This is an important result and demonstrates that these other molecular species are present and in reasonable abundances.

We are using the photosphere primarily as a source that is viewed through the shell. For this purpose, its representation is adequate. We include a little more detail in the photosphere model (i.e., a hot and a cold layer) simply to demonstrate that it is plausible that the OH and SH absorptions that are found to be present in the NIR and their corresponding emission/absorption in the IR arise from the photosphere and not the envelope. This is an important point and analysis result; otherwise, as discussed below, the abundance ratio O/C and the mass of the envelope would be quite unphysical. For the IR analysis, a two-layer model is also used that approximately accounts for the expected temperature inhomogeneity. The outer layer was treated as a transmission loss for the hot-layer emission. This is sufficient to account for the true thermal contrast imparted by both the emission and the absorption from this layer.

Provided that the distribution of rotational or vibrational states is appropriate to a single temperature, any cloud can be characterized by this temperature. In the case of V838 Mon, which is obviously a nonequilibrium, radiatively driven situation, the rotational and vibrational temperatures for a molecular band would not be expected to be exactly the same. Indeed, simultaneous fitting of the SiO fundamental and overtone features, both of which fall in the range of the IR data, is quite sensitive to vibrational temperature. A vibrational/emission temperature of 790 K is found for SiO, as opposed to the 750 K that appears to adequately characterize the H_2O and CO features.

For the specific case of V838 Mon, and particularly for the NIR, where molecular band effects dominate the RT, the simplified modeling approach is appropriate. The principal reason is that the molecular bands in the NIR are either combination or overtone/multiquantum transitions. Reemission of the initially absorbed stellar photons will overwhelmingly occur in single-quantum steps, with the corresponding wavelengths falling into the IR region, beyond $2.5 \mu\text{m}$. This means that the NIR region will function simply as an LOS transmission loss to incoming stellar photons in that spectral region. Therefore, any reasonable molecular absorption curve-of-growth band model, such as that employed in this analysis, will yield useful estimates of the absorber column amount and enable spectral shape fitting to determine the rotational temperature.

With regard to the IR analysis, if the optical depths of the gaseous species are known independently, as is the case here from the NIR analysis, then a simplified analysis approach can also be employed. In this limit, the RT solution can be formally expressed for any LOS through the envelope as a cumulative sum over the product of the local source function and local path transmittance derivative. In our analysis we assume a two-layer approximation to this integral, using the known transmittances, and *retrieve an effective source function* for the hot layer, expressed as an effective blackbody function.

The RT situation for V838 Mon is dramatically different than that for other stellar objects, such as low-mass stars, dwarfs, and giant planets (Allard et al. 1997; Burrows et al. 1997). For these objects, the RT problem involves a single object with an attached atmosphere, in which the RT is largely governed by gas at relatively high pressures. For the most part, the associated chemistry, atmospheric profiles, and RT are well described by equilibrium models. The key difference is that V838 Mon is composed of two distinct objects with very different sizes and properties. The gaseous envelope is at a very low pressure, $\sim 10^{-8}$ atm, many orders of magnitude below the characteristic pressures of the other objects. As a consequence, the RT is governed by an effective Doppler line profile due to the rather broad distribution of velocities in the multiple expansion zones, which is accounted for in our model based on observations of the velocity spread. Because of the very large difference in sizes and emitting areas of the photosphere and envelope, the photosphere dominates the spectral output of the system in the NIR and the envelope in the IR. Therefore, even though the photosphere may have a very complex, nongray spectral structure in the IR, its IR contribution beyond $\sim 4.5 \mu\text{m}$ is minor compared to that of the envelope (see Fig. 14). In the “overlap” region from ~ 2.5 – $4.5 \mu\text{m}$, we have taken into account, in an approximate but reasonable manner, the nongray nature of the photosphere. In the NIR, the spectral structure appears to be dominated by H_2O and CO transmission through the envelope, and our representation of the photosphere in terms of an effective blackbody at ~ 2100 K is sufficient for analysis of this spectrum.

There are several independent consistency checks on the model-derived parameters discussed in the paper that lend

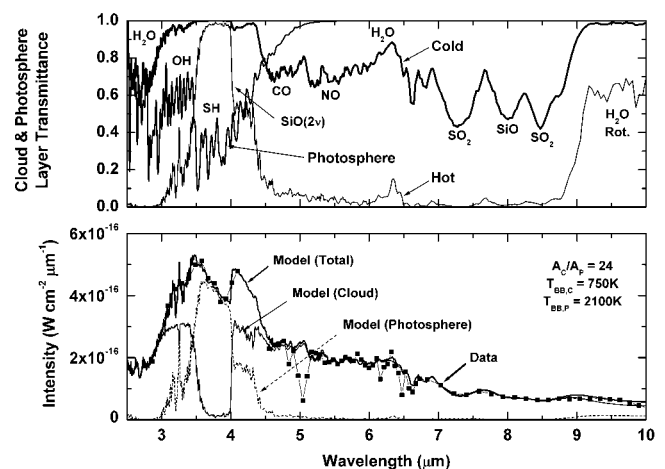


FIG. 14.—Model fit to the BASS IR flux data, showing the component transmission curves for the hot and cold layers (*top*), the component emission curves for the photosphere and cloud (*bottom*), and comparison of the model total to data (*bottom*). The identities of specific transmission features are also indicated in the top panel.

further credence to the approach. One involves predicting the effective emission temperature of the cloud on the basis of a fundamental energy conservation argument—at a steady state, the absorbed stellar energy equals the thermally emitted energy. This check only makes use of the NIR–IR spectral absorptivity/emissivity based on the derived H₂O column amount (the other species were included but are of secondary importance), the ratio of cloud and photosphere areas, and a photosphere blackbody temperature derived from the NIR data. The predicted emission temperature is 858 K, versus the 750 K derived from spectral fitting. This is reasonable accord, given the approximate nature of the modeling.

Another consistency check concerns the derived distance to V838 Mon based on the absolute radiometric output of the cloud. This involves using the results of the spectral analysis (the derived spectral transmissivity/emissivity), in conjunction with an estimate of the area of the cloud, to establish the absolute output. The area estimate is based on an assumed effective expansion velocity for the cloud. The value used for the expansion velocity was based directly on the spectral observations from a number of different groups of P Cygni profiles, indicating a spread in plausible cloud velocities in the 100–400 km s^{−1} range. We adopt 250 km s^{−1} as a representative cloud average value for the analysis but discuss the sensitivity to the uncertainty in this parameter. The derived distance is 9 kpc, versus the more precise determination of ≥6 kpc from the Hubble light-echo analysis. Again, this is reasonable accord and supports the overall plausibility of our model.

9. CONCLUSIONS

V838 Mon’s rapid transformation from a faint G or F star to a bright “later-than-M–class” star in a few months may represent a previously unobserved stage in stellar evolution, or

perhaps a new kind of star altogether. It is unquestionably oxygen-rich, as the large number of metal oxides shows. The presence of Sr II and possibly other *s*-process elements suggests that the object has evolved at least to the AGB stage and perhaps beyond. The most dramatic brightening took place in the 10 μm region, where dust formation is usually cited as the cause. There remains, however, strong evidence that the structure in this region is due to gas-phase molecules. Indeed, our model of the star and its shell suggests that the SED can be almost entirely explained without silicate dust.

We would like to thank Wayne Earthman and Keith Baker at Lick and Bill Golisch, Dave Griep, and Paul Sears at the IRTF for expert telescope operation. We also thank Daryl Kim for assistance with BASS and the observations at the IRTF. David Dearborn of Lawrence Livermore National Laboratory provided helpful discussion on the *s*-process elements. L. Bernstein acknowledges the support of Spectral Sciences, Inc. and technical discussions with R. Sundberg and A. Berk of Spectral Sciences. M. L. Sitko, D. K. Lynch, and R. W. Russell acknowledge support from NASA under grant NAG5-9475. The research of Sergio Fajardo-Acosta was carried out at the Jet Propulsion Laboratory, California Institute of Technology, and was sponsored by the National Aeronautics and Space Administration. A. Tokunaga acknowledges the support of NASA Cooperative Agreement NCC 5-538. This work was supported by The Aerospace Corporation’s Independent Research and Development program and by the United States Air Force Space and Missile Systems Center, through the Mission Oriented Investigation and Experimentation program, under contract F4701-00-C-0009.

APPENDIX

DERIVATION OF EQUATION (1)

As discussed in § 7, determination of the source function is an exceptionally complex problem for this scenario. In deriving equation (1), however, we have assumed that we already know the emission source term at each location in the cloud. The general RT equation for single-LOS emission is

$$I_{\text{los}} = \int_0^{z_m} dz B(z) (dt/dz), \quad (\text{A1})$$

where z is distance along the observer LOS, B is the blackbody source function, and t is transmittance. If we discretize this equation, assuming three homogenous layers (1 = cold, 2 = hot, 3 = stellar source), then the result is

$$I_{\text{los}} = (t_0 - t_1)B_1 + (t_1 - t_1t_2)B_2 + (t_1t_2 - t_1t_2t_3)B_3. \quad (\text{A2})$$

For this analysis we have the following simplifications: $t_0 = 1$ (boundary condition; no transmission loss from the observer to the outer layer), $B_1 = 0$ (cold/absorption-only outer layer), and $t_3 = 0$ (the star is a blackbody source). Including the area of the stellar photosphere, one obtains the total contribution of the star and the cloud emission in front of the stellar source,

$$I = A_p [t_1(1 - t_2)B_2 + t_1t_2B_3]. \quad (\text{A3})$$

As also discussed in § 3, for the analysis of the IR data it was necessary to treat the photosphere, the A_pB_3 term, as more than a simple blackbody source. We employed a two-component photosphere, with an outer emitting-absorbing layer and an inner region approximated as a blackbody source. The functional representation of this two-component photosphere (3 = outer photosphere layer and 4 = inner blackbody source region) follows by analogy to equations (A1)–(A3) and is given by

$$B_p = A_3B_3(1 - t_3) + A_4B_4t_3, \quad (\text{A4})$$

where $A_4 = A_p$, as defined in equation (A3) (i.e., we have chosen to define the size of the photosphere in terms of its blackbody source term). Here B_p replaces $A_p B_3$ in equation (A3). From equation (A4), it is seen that B_p only differs from a simple blackbody photosphere, $A_p B(T_p)$, where $t_3 < 1$. For analysis of the IR data, this only occurs in the $\sim 3.5\text{--}4\ \mu\text{m}$ region, where OH and SH emit and absorb *and* the cloud is transmissive. This enables a useful simplification to

$$B_p = A_4 B_4 [\alpha (1 - t_3) + t_3], \quad (\text{A5})$$

where

$$\alpha = \frac{A_3 B_3}{A_4 B_4}. \quad (\text{A6})$$

Because of the narrow spectral region over which OH and SH are important in the IR, to a good approximation α is constant. The utility of this approximation lies in the fact that one does not need to separately determine A_3 and B_3 , as only their product enters explicitly into the spectral fitting.

The emission from the region of the cloud *beyond* the radius of the star is given by

$$I = 2\pi \int_{R_p}^{R_c} dr \{t_1(r)[1 - t_2(r)]B_2 + t_1(r)t_2(r)[1 - t_2(r)]B_2\}. \quad (\text{A7})$$

Here r is the perpendicular/radial distance from $z = 0$, t depends on r because the segment length/optical depth of the LOS through the cloud shells is a function of r , and the second term represents the contribution of the back side of the emitting cloud layer. With a few further simplifications, $A_c \gg A_p$, $t(r) = t(r = 0)$ (i.e., the radial dependence is ignored), and combining the above stellar and cloud emission contributions, equation (1) results (note that eq. [1] is expressed as the irradiance at the observer and thus also includes the $1/R_{V838}^2$ factor).

REFERENCES

- Allard, F., Hauschildt, P. H., Alexander, D. R., & Starrfield, S. 1997, *ARA&A*, 35, 137
- Banerjee, D. P. K., & Ashok, N. M. 2002, *A&A*, 395, 161
- Bond, H. E., et al. 2003, *Nature*, 422, 405
- Brown, N. J. 2002, *IAU Circ.*, 7785, 1
- Burrows, A. M., et al. 1997, *ApJ*, 491, 856
- Crause, L. A., Lawson, W. A., Kilkenny, D., van Wyk, F., Marang, F., & Jones, A. F. 2003, *MNRAS*, 341, 785
- Desidera, S., & Munari, U. 2002, *IAU Circ.*, 7982, 1
- Duff, J. W., & Bernstein, L. S. 1981, *J. Quant. Spectrosc. Radiat. Transfer*, 26, 85
- Evans, A., Geballe, T. R., Rushton, M. T., Smalley, B., van Loon, J. Th., Eyres, S. P. S., & Tyne, V. H. 2003, *MNRAS*, 343, 1054
- Evans, A., Smalley, B., & Kimeswenger, S. 2002, *Ap&SS*, 279, 187
- Geballe, T. R., Smalley, B., Evans, A., & Rushton, M. T. 2002, *IAU Circ.*, 8016, 4
- Gillett, F. C., Forrest, W. J., Merrill, K. M., Capps, R. W., & Soifer, B. T. 1975, *ApJ*, 200, 609
- Hackwell, J. A., Warren, D. W., Dotan, Y., Lew, P. H., Lynch, D. K., Mabry, D., Russell, R. W., & Young, R. 1990, *Proc. SPIE*, 1235, 171
- Hanner, M. S., Lynch, D. K., & Russell, R. W. 1994, *ApJ*, 425, 274
- Hoffleit, D., & Jaschek, C. 1982, *The Bright Star Catalog* (4th ed.; New Haven: Yale Univ. Obs.)
- Iijima, T., & Della Valle, M. 2002, *IAU Circ.*, 7822, 1
- John, T. L. 1988, *A&A*, 193, 189
- Kammerer, A., Garcia, J., Shida, R. Y., Kiss, L., Pearce, A., & Hornoch, K. 2002, *IAU Circ.*, 7822, 2
- Kato, T. 2003, *A&A*, 399, 695
- Käuffl, H. U., Locurto, G., Kerber, F., & Heijligers, B. 2002, *IAU Circ.*, 7831, 3
- Kimeswenger, S., Lederle, C., Schmeja, S., & Armsdorfer, B. 2002, *MNRAS*, 336, L43
- Koornneef, J. 1983, *A&A*, 128, 84
- Kurucz, R. L. 1994, *Kurucz CD-ROM 19, Solar Abundance Model Atmospheres for 0, 1, 2, 4, 8 km/s* (Cambridge: SAO)
- Lynch, D. K., Russell, R. W., & Sitko, M. L. 2002a, *Icarus*, 159, 234
- Lynch, D. K., et al. 2002b, *Ap&SS*, 279, 57
- Martini, P., Wagner, R. M., Tomaney, A., Rich, R. M., della Valle, M., & Hauschildt, P. H. 1999, *AJ*, 118, 1034
- Molster, F. J., Waters, L. B. F. M., & Tielens, A. G. G. M. 2002a, *A&A*, 382, 222
- Molster, F. J., Waters, L. B. F. M., Tielens, A. G. G. M., & Barlow, M. J. 2002b, *A&A*, 382, 184
- Molster, F. J., Waters, L. B. F. M., Tielens, A. G. G. M., Koike, C., & Chihara, H. 2002c, *A&A*, 382, 241
- Munari, U., Desidera, S., & Henden, A. 2002a, *IAU Circ.*, 8005, 2
- Munari, U., et al. 2002b, *A&A*, 389, L51
- Neugebauer, G., Martz, D. E., & Leighton, R. B. 1965, *ApJ*, 142, 399
- Osiwala, J. P., Mikolajewski, M., Tomov, T., Galan, C., Nirski, J., Kolev, D., & Iliev, I. 2004, in *ASP Conf. Ser. 303, Symbiotic Stars Probing Stellar Evolution*, ed. R. L. M. Corradi, J. Mikolajewska, & T. J. Mahoney (San Francisco: ASP)
- Polonski, E. F., Telesco, C. M., Piña, R. K., & Fisher, R. S. 1999, *AJ*, 118, 2369
- Rayner, J. T., Toomey, D. W., Onaka, P. M., Denault, A. J., Stahlberger, W. E., Vacca, W. D., Cushing, M. C., & Wang, S. 2003, *PASP*, 115, 362
- Reach, W. T., Morris, P., Boulanger, F., & Okumura, K. 2003, *Icarus*, 164, 384
- Retter, A., & Marom, A. 2003, *MNRAS*, 345, L25
- Rich, R. M., Mould, J., Picard, A., Frogel, J. A., & Davies, R. 1989, *ApJ*, 341, L51
- Roche, P. F., & Aitken, D. K. 1984, *MNRAS*, 208, 481
- . 1985, *MNRAS*, 215, 425
- Rudy, R. J., Puetter, R. C., & Mazuk, S. 1999, *AJ*, 118, 666
- Sandford, S. A., & Walker, R. M., 1985, *ApJ*, 291, 838
- Sitko, M. L., Lynch, D. K., Russell, R. W., Kim, D., & Perry, R. B. 2003, *IAU Circ.*, 8078, 1
- Soker, N., & Tytenda, R. 2003, *ApJ*, 582, L105
- Speck, A. K., Barlow, M. J., Sylvester, R. J., & Hofmeister, A. M. 2000, *A&AS*, 146, 437
- Sundberg, R. L., Duff, J. W., & Bernstein, L. S. 1993, *J. Spacecraft and Rockets*, 30, 731
- Waelkens, C., Malfait, K., Waters, L. B. F. M., & De Graauw, Th. 1999, in *The Universe as Seen by ISO*, ed. P. Cox & M. F. Kessler (ESA SP-427; Noordwijk: ESA), 607
- Wagner, R. M., & Starrfield, S. G. 2002, *IAU Circ.*, 7992, 2
- Wagner, R. M., Starrfield, S. G., & Hauschildt, P. H. 2002, *BAAS*, 201, 40.02
- Walker, J., Malkmus, M., & Ludwig, C. B. 1981, *Handbook of the Standardized Infrared Radiation Model (SIRRM)*, Vol. 1: Technical Manual, Air Force Rocket Propulsion Lab. Rep. AFRPL TR 81-61 (Edwards AFB: AFRPL)
- Wright, E. L., Eisenhardt, P., & Fazio, G. 1994, *BAAS*, 184, 25.03
- Zwitter, T., & Munari, U. 2002, *IAU Circ.*, 7812, 3